ADVANCED MATERIALS
www.advmat.de

Cu/Cu$_x$O/Graphdiyne Tandem Catalyst for Efficient Electrocatalytic Nitrate Reduction to Ammonia

Xueting Feng, Jiyuan Liu, Ya Kong, Zixuan Zhang, Zedong Zhang, Shuzhou Li, Lianming Tong, Xin Gao,* and Jin Zhang**

The electrocatalytic reduction reaction of nitrate (NO_3^-) to ammonia (NH_3) is a feasible way to achieve artificial nitrogen cycle. However, the low yield rate and poor selectivity toward NH_3 product is a technical challenge. Here a graphdiyne (GDY)-based tandem catalyst featuring Cu/Cu$_x$O nanoparticles anchored to GDY support (termed Cu/Cu$_x$O/GDY) for efficient electrocatalytic NO_3^- reduction is presented. A high NH_3 yield rate of 25.4 mg h^{-1} mg$_{cat.}^{-1}$ (25.4 mg h^{-1} cm^{-2}) with a Faradaic efficiency of 99.8% at an applied potential of −0.8 V versus RHE using the designed catalyst is achieved. These performance metrics outperform most reported NO_3^- to NH_3 catalysts in the alkaline media. Electrochemical measurements and density functional theory reveal that the NO_3^- preferentially attacks Cu/Cu$_x$O, and the GDY can effectively catalyze the reduction of NO_2^- to NH_3. This work highlights the efficacy of GDY as a new class of tandem catalysts for the artificial nitrogen cycle and provides powerful guidelines for the design of tandem electrocatalysts.

1. Introduction

Ammonia (NH_3), a critical feedstock for nitrogen fertilizers and a potential hydrogen carrier, is industrially produced by the energy and carbon-emission intensive Haber–Bosch process.[1] Alternatively, electrocatalytic nitrogen reduction reaction (NRR) can be driven by renewable energy under mild conditions using water as the hydrogen source. However, the NH_3 yield rate by NRR is two orders of magnitude lower than Haber–Bosch process, due to the low solubility and high dissociation energy (941 kJ mol^{-1}) of nitrogen.[2] Recently, the production of NH_3 from nitrogen via a nitrate (NO_3^-) intermediate with a lower dissociation energy (204 kJ mol^{-1}) has been demonstrated to be a promising way to improve NH_3 yield rate and Faradaic efficiency (FE).[3] Additionally, NO_3^-, as a ubiquitous water contaminant, can be directly reduced to generate NH_3 for restoring the imbalance in the global nitrogen cycle.[4] However, this strategy suffers from poor activity and selectivity due to its complex eight-electron reduction process and competitive hydrogen evolution.[5] Therefore, it is crucial to rationally design and construct efficient electrocatalysts to improve activity and energy conversion efficiency for electrocatalytic nitrate reduction reaction (NO_3RR).

Copper (Cu) catalyst with a unique 3d electron orbital shows excellent ability to bind NO_3^- and catalyze the conversion of NO_3^- to NO_2^-.[6] However, pure Cu particles are usually rapidly deactivated by strong adsorption of NO_3RR intermediates (such as NO_2^- and NO), and the efficiency of NO_2^- to NH_3 conversion with pure Cu catalyst is very low.[7] The Cu/Cu$_2$O heterojunction was fabricated to enhance catalytic activity, which can effectively regulate the electronic structure at interface and then alleviated adsorption energy of NO_2^- owing to the synergistic effect.[6a,8] More recently, "tandem catalysis" was developed to further improve catalytic activity and selectivity by introducing other active substances. In the core–shell Cu/Cobalt (Co) tandem catalyst, the internal Cu/CuO$_x$ preferentially catalyzes the reduction of NO_3^- to NO_2^-, and NO_2^- is quickly reduced to NH_3 in the nearby Co/CoO.[9] A high NH_3 yield rate (1.17 mmol cm^{-2} h^{-1}) and FE (93.3 ± 2.1%) were achieved. Despite these improvements in the tandem catalyst design, study on improving the NO_3RR kinetics using the tandem catalyst are still in their infancy. The poor chemistry between NO_2^- and NH_3 still need to be addressed. Specifically, the Faradaic efficiency higher than 99% is highly pursued for achieving artificial nitrogen cycle.

Graphdiyne (GDY) is a new 2D carbon allotrope composed of sp2 and sp-hybridized carbon atoms with uniform pores and highly π-conjugated structure.[10] Its unique structures render GDY with multiple advantages in electrocatalysis.[11] The

X. Feng, Y. Kong, Z. Zhang, Z. Zhang, L. Tong, X. Gao, J. Zhang
Beijing National Laboratory for Molecular Sciences
Beijing Science and Engineering Center for Nanocarbons
College of Chemistry and Molecular Engineering
School of Materials Science and Engineering
Peking University
Beijing 100871, P. R. China
E-mail: tonglm@pku.edu.cn; gaoxin-cnc@pku.edu.cn; jinzhang@pku.edu.cn
J. Liu, S. Li
School of Materials Science and Engineering
Nanyang Technological University
Singapore 639798, Singapore
Z. Zhang
Department of Chemistry
Tsinghua University
Beijing 100084, P. R. China

The ORCID identification number(s) for the author(s) of this article can be found under https://doi.org/10.1002/adma.202405660

DOI: 10.1002/adma.202405660

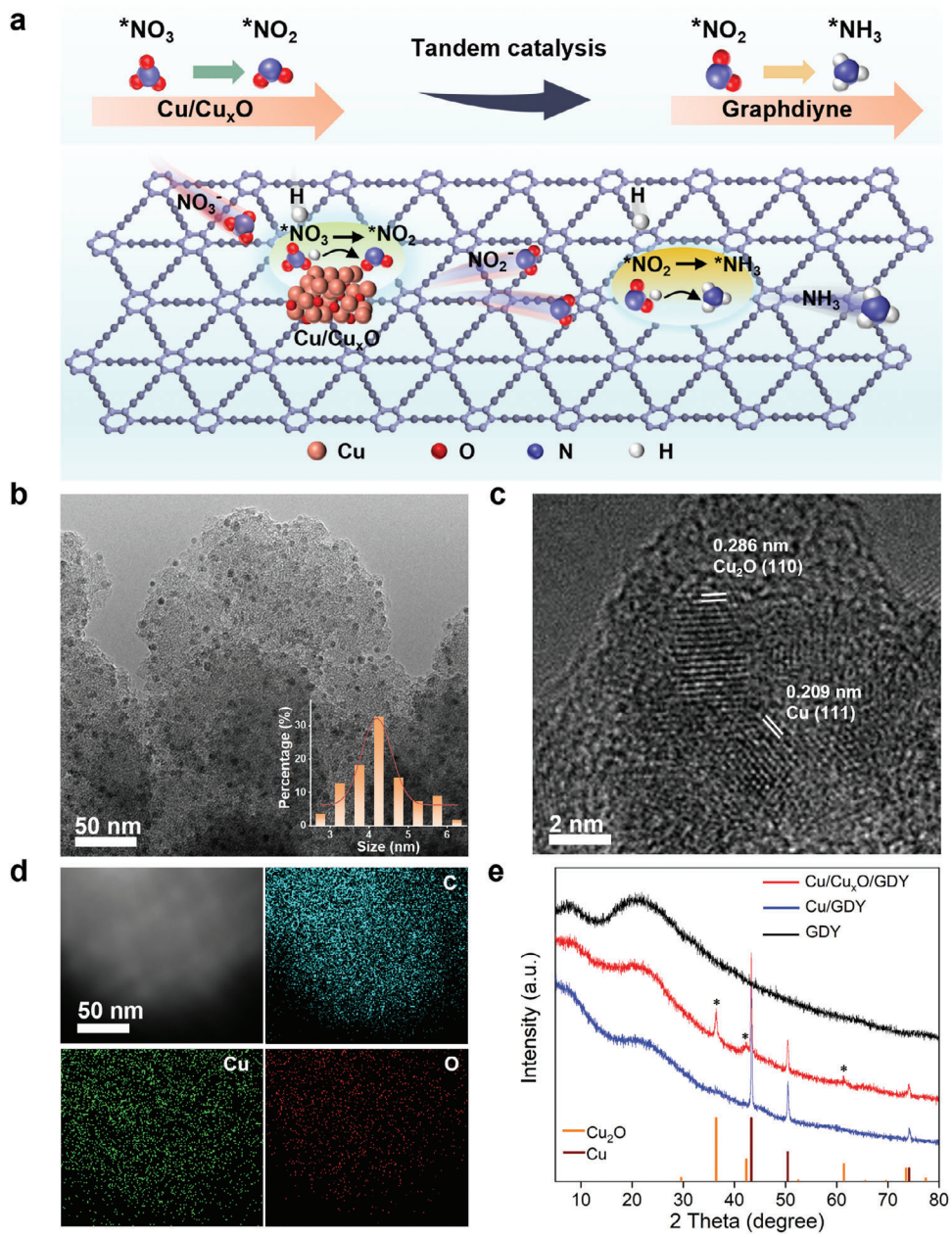

Figure 1. Conceptual diagram of NO_3RR on $Cu/Cu_xO/GDY$ and characterizations of $Cu/Cu_xO/GDY$. a) Proposed reaction scheme for NO_3RR on $Cu/Cu_xO/GDY$. b) Transmission electron microscopy (TEM) image of $Cu/Cu_xO/GDY$. Inset: corresponding particle size distribution. c) High-resolution TEM (HRTEM) image of $Cu/Cu_xO/GDY$. d) High-angle annular dark-field scanning transmission electron microscopy (HAADF-STEM) image and corresponding EDX elemental mapping images of $Cu/Cu_xO/GDY$. e) X-ray diffraction (XRD) patterns of $Cu/Cu_xO/GDY$, Cu/GDY, and GDY.

sub-nanometer pores favor the ion transport. Uneven surface charge distribution facilitates the selective adsorption of the intermediates.[12] The uneven distribution of surface charge in GDY gives it high intrinsic catalytic activity for generating hydrogen radicals (H•) from the electrolyte.[13] We hypothesize that GDY can be used as a new class of tandem catalysts for the artificial nitrogen cycle.

Here, we report a catalyst featuring Cu/Cu_xO nanoparticles supported on GDY termed $Cu/Cu_xO/GDY$ (**Figure 1a**). The experimental and theoretical results reveal that the NO_3^- preferentially attacks Cu/Cu_xO, and the GDY can effectively catalyze the reduction of NO_2^- to NH_3. The NO_3RR using $Cu/Cu_xO/GDY$ shows a tandem catalytic mechanism, in which the reduction of NO_3^- to NO_2^- preferentially occurs at the Cu/Cu_xO species site of the catalyst, and then the escaped NO_2^- is captured by GDY and converted into NH_3. Electrochemical measurements demonstrate that the $Cu/Cu_xO/GDY$ shows a high NH_3 yield rate of 25.4 mg h^{-1} $mg_{cat.}^{-1}$ with a FE of 99.8% at an applied potential of −0.8 V versus RHE. Moreover, the $Cu/Cu_xO/GDY$ tandem catalyst shows the high FE (>90%) at wide potential range of −0.6

to −0.9 V. We believe that incorporating novel carbon allotrope GDY as the tandem catalyst for efficient electrocatalytic NO_3^- reduction represents a new and exciting direction.

2. Results and Discussion

2.1. Synthesis and Characterization of the Cu/Cu_xO/GDY Tandem Catalyst

The Cu/Cu_xO/GDY catalyst was obtained by direct reduction of Cu-precursor/GDY though a solvothermal method (Figure S1, Supporting Information). Briefly, the Cu-precursor/GDY was synthesized via alkynylsilane coupling reaction using a microware-assisted wet chemistry method, which involves the coupling reaction of the monomer hexakis[(trimethylsilyl)-ethynyl]benzene (HEB-TMS) in *N,N*-dimethyformamide (DMF) using copper chloride (CuCl) as the catalyst.[14] The as-prepared Cu-precursor/GDY shows a circular nanosheet structure with an average diameter of 250 nm and thickness of 2.35 nm (Figure S2a–c; and Figure S3, Supporting Information). The area with thickness of 12.4 nm is speculated to be a nucleation center, which is similar to the nucleation center that appeared during the growth process of GDY films in previous work.[15] Figure S2c (Supporting Information) shows the interlayer of GDY (0.367 nm). Cu, C, Cl, and O elements are uniformly distributed throughout the Cu-precursor/GDY (Figure S2d, Supporting Information). The content of Cu in the catalysts is 13.4% determined by the inductively coupled plasma-optical emission spectrometer (ICP-OES). Subsequently, the Cu/Cu_xO/GDY with the Cu content of 12.7% was synthesized by a solvothermal method. The facile, scalable nature, and low costs of reagents of the Cu/Cu_xO/GDY synthesis method endow the GDY-based catalyst with promise for large-scale commercialization. As-prepared Cu/Cu_xO/GDY remained circular nanosheet structure. The Cu/Cu_xO nanoparticles are uniformly distributed on the GDY scaffold with an average diameter of 4.32 nm (Figure 1b). In the high-resolution TEM (HRTEM) image, the lattice spacing of 0.286 and 0.209 nm are attributed to the (110) plane of Cu_2O and the (111) plane of Cu (Figure 1c). The elements of C, Cu, and O are uniformly distributed throughout the Cu/Cu_xO/GDY according to the energy-dispersive X-ray spectroscopy (EDX) mapping results (Figure 1d). For comparison, the Cu nanoparticles on GDY nanosheets (Cu/GDY) and pure GDY nanosheets control sample were also synthesized. The Cu content in the Cu/GDY is 11.4 wt%. The Cu nanoparticles (with an average diameter of 5.55 nm) are evenly dispersed on the GDY matrix, and the lattice spacing of 0.209 nm is assigned to the (111) plane of Cu (Figure S4a–c, Supporting Information). The GDY shows the circular nanosheet morphology and the uniform distribution of C and O (Figure S5, Supporting Information). A small amount of copper residue in the GDY (≈0.13 wt%) was revealed by ICP-OES and X-ray photoelectron spectroscopy (XPS) (Figure S6, Supporting Information). The crystal structure of Cu/Cu_xO/GDY, Cu/GDY, and GDY were further demonstrated by X-ray diffraction (XRD) in Figure 1e. There are broad peaks over 23° in all three samples, which belong to the interlayer distance of GDY.[16] The characteristic peaks in Cu/Cu_xO/GDY are attributed to Cu (PDF no. 04-0836) and Cu_2O (PDF no. 05-0667), further demonstrating the existence of Cu and Cu_2O in Cu/Cu_xO/GDY. The obvious peak of metallic Cu can be observed in Cu/GDY.

The structure of obtained samples was further investigated by XPS, Raman spectroscopy, and X-ray absorption spectroscopy (XAS). The XPS survey spectrum further confirmed the presence of Cu, C, Cl, and O elements (Figure S7a, Supporting Information).The XPS C 1s spectrum of Cu-precursor/GDY shows four peaks at 284.4, 285.0, 286.4, and 288.5 eV, which is ascribed to C—C (sp^2), C—C (sp), C—O, and C═O, respectively (Figure S7b, Supporting Information).[17] The ratio of sp to sp^2 carbon atoms is calculated to 2, which is consistent with theoretical value of the GDY structural. XPS analysis reveals the presence of Cu^{2+} and Cu^+ on the surface of Cu-precursor/GDY. In Figure S7c (Supporting Information), the peaks of Cu $2p_{3/2}$ and Cu $2p_{1/2}$ at 932.5 and 952.3 eV are assigned to Cu^+ or Cu^0,[18] while two peaks appeared at 934.1 and 953.8 eV are attributed to Cu^{2+}.[19] Auger electron spectroscopy (AES) was used to distinguish Cu^0 and Cu^+, and the results showed that the signal was mainly came from Cu^+ (Figure S7d, Supporting Information). The Cu/Cu_xO/GDY and Cu/GDY were obtained by reducing Cu-precursor/GDY for different times. The Cu 2p XPS spectra and the Cu LMM AES spectra show the presence of Cu^0, Cu^+, and Cu^{2+} in Cu/Cu_xO/GDY, and the presence of Cu^0 in Cu/GDY (**Figure 2**a,b; and Figure S8a,b, Supporting Information), and the results are consistent with XRD. Correspondingly, the Cu 2p peaks of Cu/Cu_xO/GDY shifts to lower binding energy than that of Cu/GDY, revealing the electron redistribution at the Cu/Cu_xO/GDY interface. Figure 2c shows Raman spectra of Cu/Cu_xO/GDY, Cu/GDY, and GDY. The different peaks at 1384.7 and 1585.5 cm^{-1} are attributed to the D band and G band of GDY, respectively. The peak located at 2163.4 cm^{-1} is assigned as the triple bond vibration of the conjugated diyne linkage (—C≡C—C≡C—) in GDY. X-ray absorption fine structure (XAFS) was carried out to further monitor the structure of Cu in the Cu/Cu_xO/GDY, with Cu foil, Cu_2O and CuO as reference. The near-edge absorption energy of Cu/Cu_xO/GDY locates between Cu foil and Cu_2O references, implying the coexistence of Cu^0 and Cu^+ (Figure 2d; and Figure S9, Supporting Information). The comparison of k^3-weighted EXAFS paths is exhibited in Figure S10 (Supporting Information). The results of X-ray absorption near-edge spectroscopy (XANES) deconvolution fitted by a linear combination of Cu^0, Cu^+, and Cu^{2+} spectra confirm the presence of three valence states of Cu, and the results are consistent with XPS analysis (Figure 2e). As shown in Fourier transformed k^3-weighted extended XAFS (FT-EXAFS, without phase correction) spectra, two peaks of Cu/Cu_xO/GDY at ≈1.5 and 2.2 Å are ascribed to the Cu—O and Cu—Cu superimposed contribution, respectively (Figure 2f).[20]

2.2. Electrocatalytic Nitrate Reduction Performance

TheNO_3RR was assessed in a customized H-cell containing 1 M KOH and 0.1 M KNO_3 at room temperature. The as-prepared catalysts were loaded on the carbon paper (CP) with a mass loading of 1 mg cm^{-2}. Linear sweep voltammetry (LSV) was employed to examine the effect of Cu/Cu_xO/GDY on the NO_3^- reduction kinetics. **Figure 3**a shows that the Cu/Cu_xO/GDY in the presence of NO_3^- exhibits a greatly increased current response compared to that without NO_3^-, revealing the high

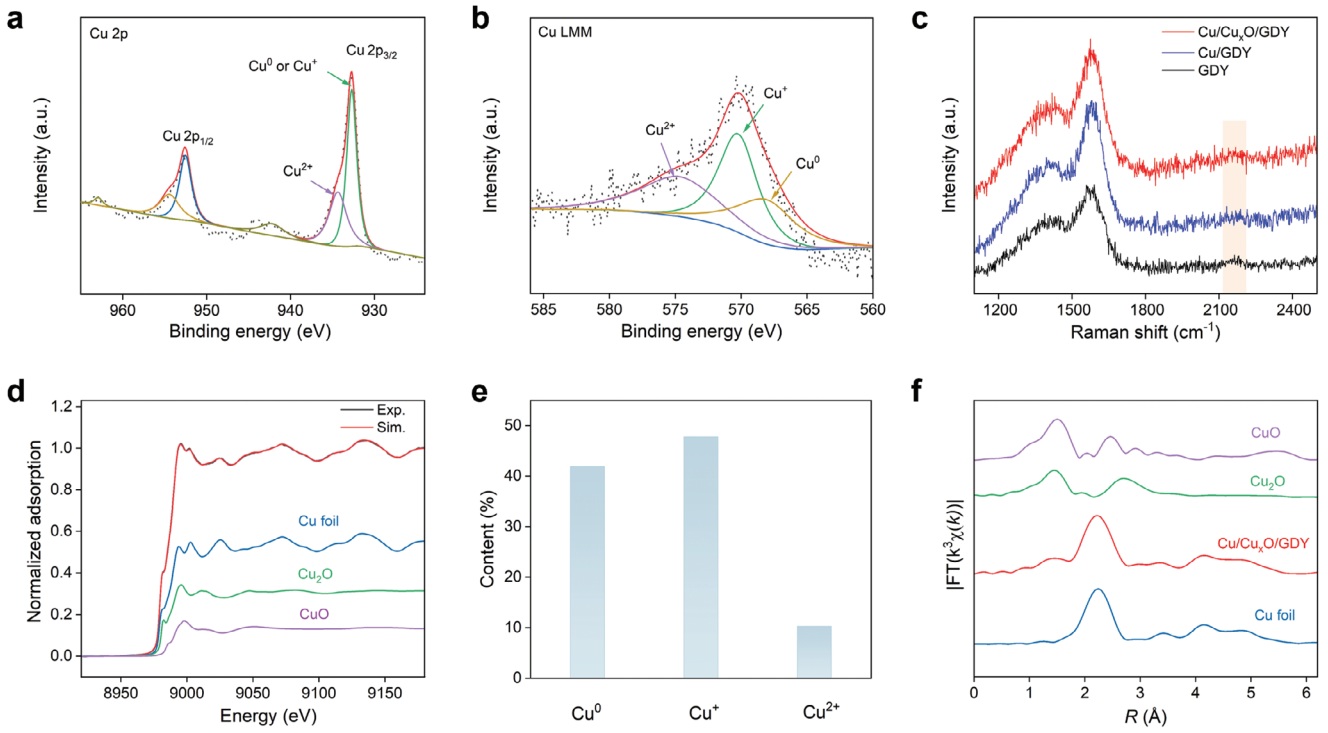

Figure 2. Structural analysis of Cu/Cu$_x$O/GDY. a) The high-resolution Cu 2p XPS and b) Cu LMM AES spectra of Cu/Cu$_x$O/GDY. c) Raman spectra of Cu/Cu$_x$O/GDY, Cu/GDY, and GDY. d) X-ray absorption near-edge structure (XANES) spectra at the Cu K-edge of Cu/Cu$_x$O/GDY, referenced Cu foil, Cu$_2$O, and CuO. The red line in Figure 2d is the linear combination fitting of Cu K-edge XANES. e) The content fraction of Cu^0, Cu$^+$, Cu^{2+} of Cu/Cu$_x$O/GDY. f) Fourier transformed (FT) k^3-weighted $\chi(k)$-function of the EXAFS spectra at the Cu K-edge of Cu/Cu$_x$O/GDY, referenced Cu foil, Cu$_2$O, and CuO.

NO_3RR activity of Cu/Cu$_x$O/GDY. The NO_3RR process was analyzed by chronoamperometry measurement, and the liquid products (NH_3 and NO_2^-) were quantified by spectrophotometric method.[21] The corresponding calibration curves are shown in Figures S11 and S12 (Supporting Information). The CP substrate is inactive for electrochemical NO_3RR activity, which suggests the important role of supported catalyst (Figure S13, Supporting Information). As shown in Figure 3b, the NH_3 yield rate gradually increases, and the highest value can reach up to 33.9 mg h^{-1} mg$_{cat.}^{-1}$ (33.9 mg h^{-1} cm^{-2}) at −0.9 V. Strikingly, the Faradaic efficiency (FE) exhibits volcanic distribution with the highest value of 99.8% at an applied potential of −0.8 V versus RHE, while the NH_3 yield rate can reach 25.4 mg h^{-1} mg$_{cat.}^{-1}$ at −0.8 V. Additionally, the highest FE values above 90% are also achieved in wide potential range of −0.6 to −0.9 V. As the applied potentials increases, the concentration of NO_2^- products decreases, whereas the concentration of NH_3 produce increases, indicating the high selectivity to NH_3 (Figure S14, Supporting Information). As shown in Figure 3c, the partial current density increases with increasing applied potential, and the highest value of 385.0 mA cm^{-2} over Cu/Cu$_x$O/GDY is ≈2.3 times higher than that of Cu/GDY (170.5 mA cm^{-2}). To further evaluate the NO_3RR activity of the catalyst, the partial current density of NH_3 was normalized by the electrochemically active surface area (ECSA).[22] A similar trend was observed, and the maximum ECSA normalized current density was achieved on Cu/Cu$_x$O/GDY (Figure S16, Supporting Information). The above results reveal that the Cu/Cu$_x$O/GDY possesses superior intrinsic NO_3RR activity. The ECSA of Cu/Cu$_x$O/GDY is larger than that of Cu/GDY, indicating more exposed active sites for Cu/Cu$_x$O/GDY (Figure S15, Supporting Information). Nuclear magnetic resonance (NMR) was performed to test the reliability of spectrophotometric quantitative detection of NH_3. The corresponding calibration curves were shown in Figures S17 and S18 (Supporting Information). The NH_3 yield rate and FE analyzed by NMR are 25.8 mg h^{-1} mg$_{cat.}^{-1}$ and 99.8% at −0.8 V for Cu/Cu$_x$O/GDY (Figure 3d), which is consistent with the results of spectrophotometric method (25.4 mg h^{-1} mg$_{cat.}^{-1}$ and 99.8%), indicating the reliability of quantitative tests. Furthermore, isotope labeling experiments were performance by the NMR method to confirm the N source and accurately quantify the NH_3 product from Cu/Cu$_x$O/GDY during NO_3RR. The electrolyte with 0.05 M $K^{15}NO_3$ and 0.05 M $K^{14}NO_3$ is used. The ^{1}H NMR spectra (Figure 3e) show triple and doublet signals using $^{14}NO_3^-$ and $^{15}NO_3^-$ as N source, corresponded to $^{14}NH_4^+$ and $^{15}NH_4^+$, respectively.[23] There is no signal of $^{14}NH_4^+$ during the electrolysis of $^{15}NO_3^-$, eliminating the influence of NH_3 pollution. The NH_3 yield rate and FE are 14.6 mg h^{-1} mg$_{cat.}^{-1}$ and 97.0% at −0.8 V using $^{14}NO_3^-$ as N source and 14.5 mg h^{-1} mg$_{cat.}^{-1}$ and 94.0% using $^{15}NO_3^-$ as N source at −0.8 V. Moreover, the NO_3RR activity of Cu/Cu$_x$O/GDY are also evaluated in 0.01 M KNO_3 and 0.05 M KNO_3 due to the different concentration in various sources. The maximal FE value of 98.6 and 97.0% are achieved in 0.01 M KNO_3 and 0.05 M KNO_3, suggesting that the Cu/Cu$_x$O/GDY catalyst can effectively catalyze the NO_3^- to NH_3 conversion in different nitrates (Figure S19, Supporting

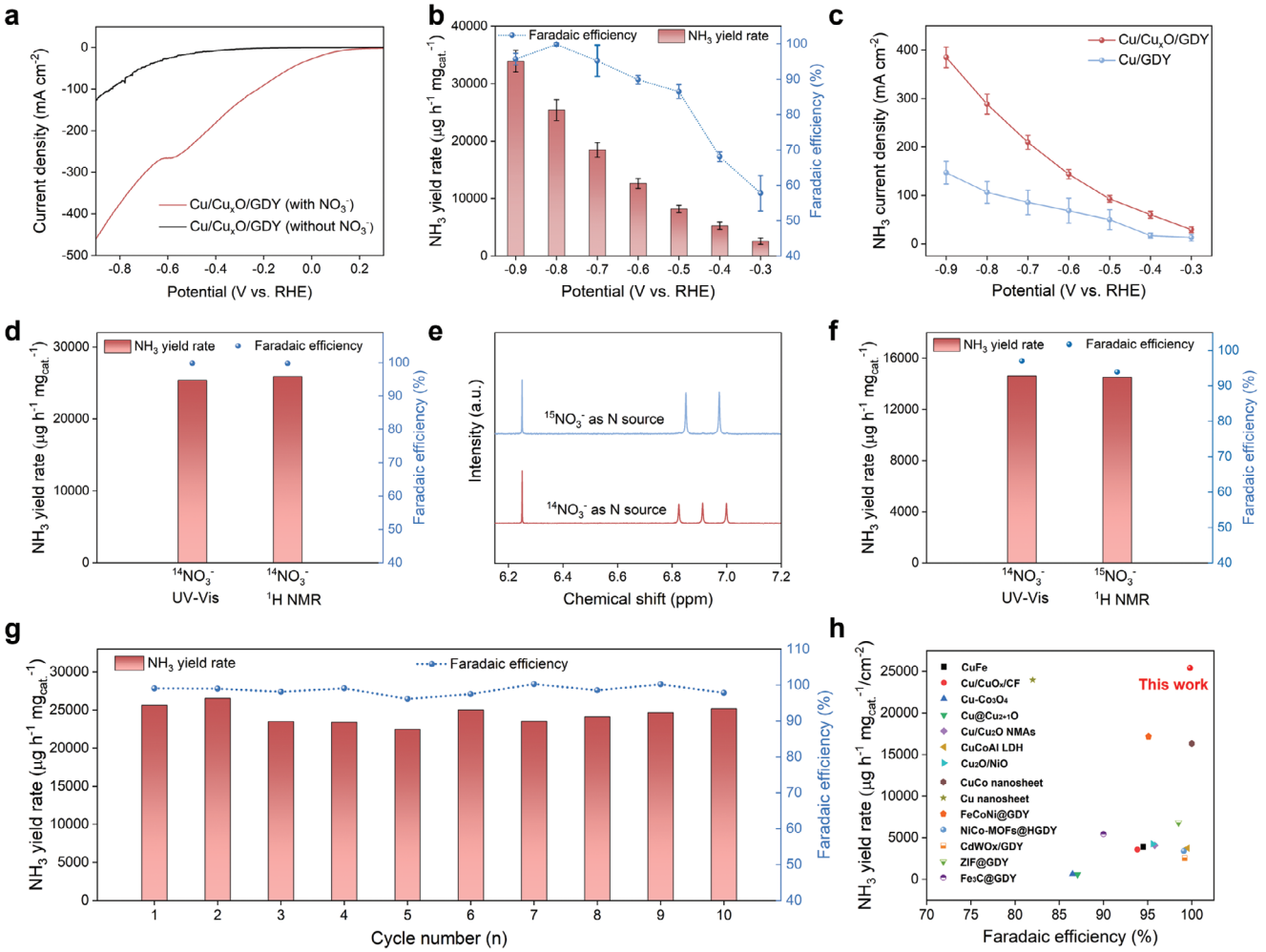

Figure 3. Electroreduction of NO_3^- to NH_3 under ambient conditions. a) LSV curves of Cu/Cu_xO/GDY in 1 M KOH with and without NO_3^-. b) NH_3 yield rate and Faradaic efficiency (FE) of Cu/Cu_xO/GDY at selected potentials. c) NH_3 current densities of NO_3RR at different applied potentials of Cu/Cu_xO/GDY and Cu/GDY. d) Comparison of the calculated NH_3 yield rate and FE at −0.8 V in 0.1 M KNO3 by NMR and UV–vis methods. e) ^{1}H NMR spectra of the NO_3RR products using different feed. f) Comparison of the calculated NH_3 yield rate and FE at −0.8 V in 0.05 M KNO_3 fed by $^{14}NO_3^-$/$^{15}NO_3^-$ by NMR and UV–vis methods. g) Cycling test of Cu/Cu_xO/GDY at −0.8 V. h) Comparisons of NO_3RR performance of Cu/Cu_xO/GDY with other reported electrocatalysts.

Information). The enhancing NH_3 yield rate are observed by increasing the concentrations from 0.01 to 0.1 M (Figure S20, Supporting Information). The enhanced NO_3RR activity of Cu/Cu_xO/GDY was also verified by electrochemical impedance spectroscopy (EIS) measurement. The impedance spectra were fitted by the EC-Lab Software (Figure S21, Supporting Information). Compared with the Cu/GDY and the GDY catalyst, designed Cu/Cu_xO/GDY catalyst shows the smallest charge transfer resistance (R_{ct}) of 5.8 Ω, which facilitates the charge transfer for NO_3RR and thus improves the reaction kinetics. Additionally, the NH_3 yield rate and FE of Cu/Cu_xO/GDY remain stable through ten consecutive tests, revealing the excellent electrochemical durability (Figure 3g). Such NH_3 yield rate and FE obtained simultaneously at −0.8 V outperforms the reported catalysts (Figure 3h; and Table S1, Supporting Information).[6a,c,d,9,23–24] The TEM images and Raman spectrum present the morphology of the Cu/Cu_xO/GDY and the structure of GDY maintains well after cycling test (Figures S22 and S23a, Supporting Information). The XPS spectra (Figure S23b,c, Supporting Information) and XAS spectra (Figure S24, Supporting Information) show that the Cu/Cu_xO/GDY is composed of Cu^{2+}, Cu^+ and Cu^0 after cycling test. The ICP-OES analysis further reveals the excellent stability of the Cu/Cu_xO/GDY catalyst (Table S2, Supporting Information). The above results indicate that Cu/Cu_xO/GDY has high FE and NH_3 yield rate and excellent stability.

2.3. The Mechanism of Electrocatalytic NO_3RR

To further elucidate the mechanism of NO_3RR on the Cu/Cu_xO/GDY, the roles of Cu species and GDY were investigated. **Figure** 4a shows that the NH_3 yield rate of Cu/Cu_xO/GDY is significantly higher than that of Cu/GDY under various

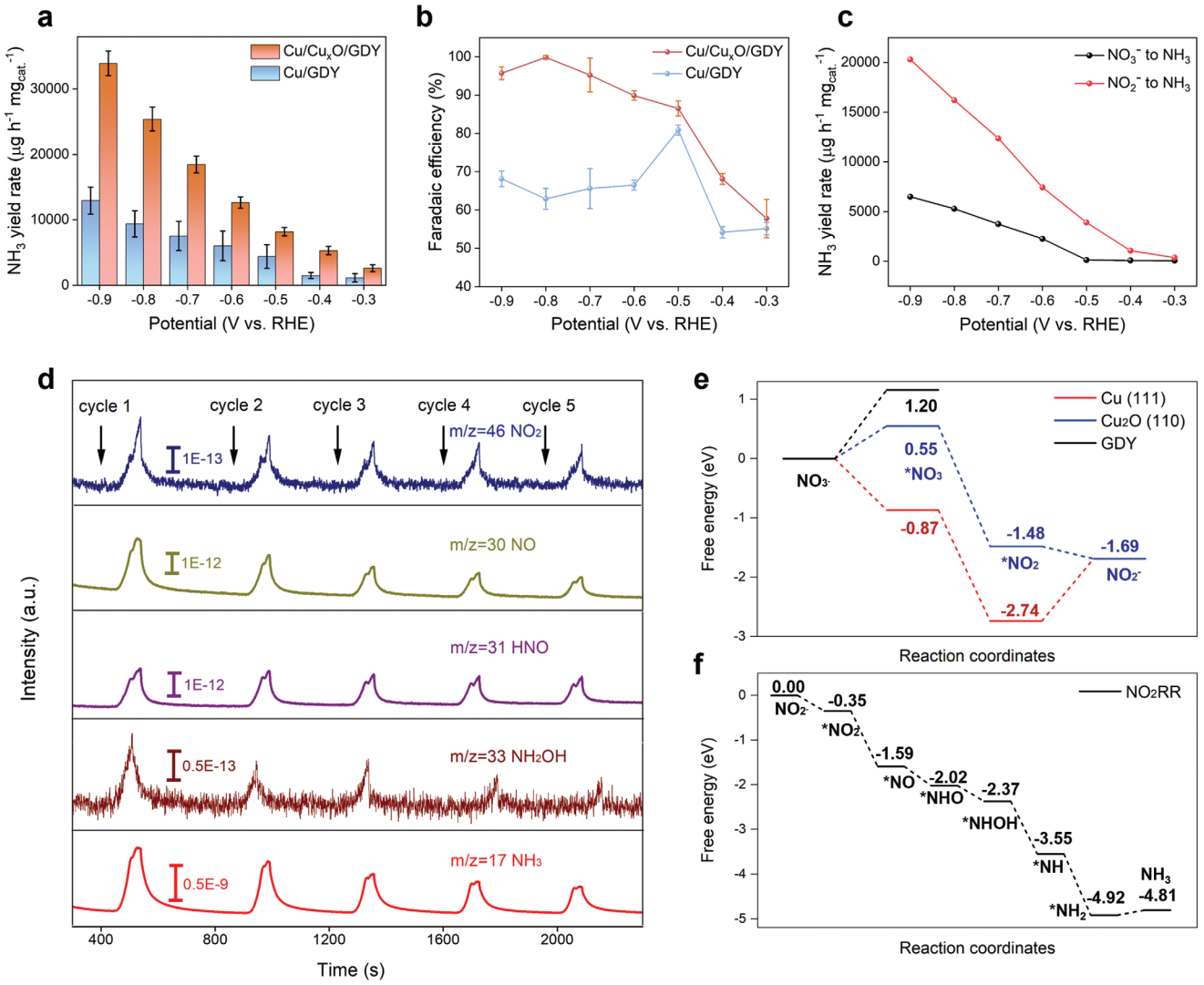

Figure 4. The mechanism of NO_3RR on Cu/Cu$_x$O/GDY. a) NH_3 yield rate and b) Faradaic efficiency (FE) of Cu/Cu$_x$O/GDY and Cu/GDY at selected potentials. c) NH_3 yield rate of GDY for NO_3^- and NO_2^- reduction. d) The online DEMS measurements of NO_3RR on Cu/Cu$_x$O/GDY. e) Free energy diagrams of NO_3^--to-*NO_2 conversion and the escape of NO_2^- on Cu, Cu_2O, and GDY at U = −0.8 V. f) Free energy diagrams of NO_2^--to-NH_3 conversion on GDY at U = −0.8 V.

applied potentials, with the value of Cu/Cu$_x$O/GDY being nearly 27.0 times greater than that of Cu/GDY at −0.8 V. The maximum FE value of Cu/Cu$_x$O/GDY is 1.2 times higher than that of Cu/GDY (Figure 4b). Besides, the Cu/Cu$_x$O/GDY catalyst can simultaneously achieve high NH_3 yield rate and FE at the same potential. The above results reveal that the important role of Cu$_x$O in improving the electrocatalytic NO_3^--to-NH_3 conversion activity. Compared with pure GDY (Figure 4c), both Cu/Cu$_x$O/GDY and Cu/GDY with high NH_3 yield rate show excellent NO_3RR activity, revealing that the Cu species are dominant active site for NO_3RR. Further, we want to point out that the GDY can effectively catalyze the reduction of NO_2^- to generate NH_3. The NH_3 yield rate significantly increases in different potential regions when NO_3^- is replaced by NO_2^- when we used the GDY as the catalyst. Therefore, based on the above analysis, we speculate that the NO_3RR process for Cu/Cu$_x$O/GDY involves a tandem catalytic mechanism. During the NO_3RR electrolysis process, the reduction of NO_3^- to NO_2^- preferentially occurs at the Cu species site of the catalyst, and then the escaped NO_2^- is captured by GDY and converted into NH_3. To further illustrate the efficacy of the tandem catalyst concept, we prepared Cu/Cu_2O (Figure S25, Supporting Information) and evaluated its electrocatalytic NO_3RR performance. Compared with Cu/Cu_2O and GDY catalyst, the tandem catalyst Cu/CuO$_x$/GDY shows excellent performance with high NH_3 yield rate and FE (Figure S26, Supporting Information). To reveal the possible reaction pathway, online differential electrochemical mass spectrometry (DEMS) was performed to detect the molecular intermediates during the NO_3RR process. Figure 4d shows the mass to charge (m/z) ratio when five subsequent voltammetry scan cycles were performed with the voltage from 0.2 to −0.9 V. The m/z signal of 46, 30, 31, 33, and

17 are corresponded to NO_2, NO, HNO, NH_2OH, and NH_3, respectively.

To attain an in-depth understanding of the catalytic effect of Cu/Cu_xO/GDY for improved charge reaction kinetics in NO_3RR, the overall reaction mechanism for NO_3RR is simulated. First-principles calculations propose detailed energetics and kinetics of reaction steps for the Cu/Cu_xO/GDY-modulated NO_3^- reduction. Cu (111) and Cu_2O (110) were identified as the dominantly exposed facets, according to the HRTEM results (Figure 1c). The NO_3^- adsorption and activation were first investigated on these catalyst surface. The NO_3^- adsorption on GDY owns a particularly high adsorption free-energy of 1.20 eV, which accounts for the observed poor NO_3RR performance on GDY in our experiments (Figure 4c,e; and Figure S28, Supporting Information). At the Cu (111) active site, the NO_3^- could easily adsorb and be reduced to $*NO_2$ intermediate (Figure 4e; and Figure S29, Supporting Information). However, this $*NO_2$ intermediate tends to remain at the active site, impeding the generation of the NO_2^- species. In contrast, the Cu_2O (110) exhibits a moderate NO_3^- adsorption free-energy of 0.55 eV, facilitating a downhill pathway to NO_2^- formation (Figure 4e; and Figure S30, Supporting Information). The potential-determining step (PDS) for NO_3^- adsorption and activation is thus identified as the NO_3^- adsorption on Cu_2O (110). This also demonstrates that the first step of NO_3RR process is triggered by Cu species rather than the GDY components. Furthermore, the reaction of nitrite reduction to ammonia was theoretically investigated as well (Figure 4f). The predicted pathway suggests the $*NO_2$ is sequentially reduced to *NO, *NHO, *NHOH, and NH_3 with assistance from the adsorbed H atom (Figures S31 and S32, Supporting Information), which perfectly aligns with our online DEMS results. The PDS of NO_2RR on GDY is the generation of NH_3 with the ΔG much lower than that on Cu_2O, suggesting the NO_2^- can be easily absorbed and converted to NH_3 on GDY. The whole process is that NO_3^- is preferentially adsorbed on the Cu species site of the catalyst and reduced to NO_2^-, and then the escaped NO_2^- is captured by GDY and converted into NH_3. Consequently, the tandem catalytic mechanism leads to the improved NH_3 yield rate and FE on Cu/Cu_xO/GDY.

3. Conclusion

In summary, we have developed a Cu/Cu_xO/GDY catalyst that improves the redox kinetics and the stability of NO_3RR. Using experiments and DFT calculations, we demonstrate that the Cu/Cu_xO/GDY greatly improves the electrocatalytic conversion activity and selectivity of NO_3RR. GDY provide active sites for the reduction of NO_2^- to generate NH_3. Electrochemical measurements show that the superior nitrate to ammonia conversion is maintained at different potentials. The Cu/Cu_xO/GDY catalyst achieved a FE as high as 99.8% and a yield rate of 25.4 mg h^{-1} $mg_{cat.}^{-1}$, which outperforms the reported catalysts. Our designed catalyst opens up new possibilities for designing non-metallic tandem electrocatalysts with high activity and selectivity.

Supporting Information

Supporting Information is available from the Wiley Online Library or from the author.

Acknowledgements

This work was financially supported by the Ministry of Science and Technology of China (No. 2018YFA0703502), the National Natural Science Foundation of China (Grant Nos. 52302034, 52021006, and 21974004), the Strategic Priority Research Program of CAS (No. XDB36030100), and the Beijing National Laboratory for Molecular Sciences (No. BNLMS-CXTD-202001), the Shenzhen Science and Technology Innovation Commission (No. KQTD20221101115627004), the China Postdoctoral Science Foundation (Grant Nos. 8206300625 and 8206400103), the Academic Research Fund Tier 1 (No. RG10/21), Academic Research Fund Tier 2 (No. MOE-T2EP10220-0005), and Academic Research Fund Tier 2 (No. MOE-T2EP20221-0003). The authors thanked the computing resources from National Supercomputing Centre Singapore.

Conflict of Interest

The authors declare no conflict of interest.

Author Contributions

X.T.F. and J.Y.L. contributed equally to this work. X.F., L.T., X.G., and J.Z. conceived and designed the investigation. X.F. conducted the GDY and catalyst synthesis, electrochemical measurements, and material characterizations. J.L. and S.L. performed DFT calculations. Y.K. and Z.Z. assisted with the material synthesis. Z.Z. helped the analysis of XAFS results. L.T., X.G., and J.Z. supervised the project. X.F., J.L., and X.G. co-wrote the paper. All authors discussed the results and commented on the manuscript.

Data Availability Statement

The data that support the findings of this study are available from the corresponding author upon reasonable request.

Keywords

electrocatalysis, graphdiyne, nitrate reduction, tandem catalysts

Received: April 21, 2024
Revised: May 23, 2024
Published online:

[1] G.-F. Chen, Y. Yuan, H. Jiang, S.-Y. Ren, L.-X. Ding, L. Ma, T. Wu, J. Lu, H. Wang, *Nat. Energy* **2020**, *5*, 605.
[2] a) J. G. Chen, R. M. Crooks, L. C. Seefeldt, K. L. Bren, R. M. Bullock, M. Y. Darensbourg, P. L. Holland, B. Hoffman, M. J. Janik, A. K. Jones, M. G. Kanatzidis, P. King, K. M. Lancaster, S. V. Lymar, P. Pfromm, W. F. Schneider, R. R. Schrock, *Science* **2018**, *360*, 873; b) F. Jiao, B. Xu, *Adv. Mater.* **2019**, *31*, 1805173.
[3] a) J. John, D. R. MacFarlane, A. N. Simonov, *Nat. Catal.* **2023**, *6*, 1125; b) L. Li, C. Tang, X. Cui, Y. Zheng, X. Wang, H. Xu, S. Zhang, T. Shao, K. Davey, S. Z. Qiao, *Angew. Chem., Int. Ed.* **2021**, *60*, 14131.
[4] a) J. Li, G. Zhan, J. Yang, F. Quan, C. Mao, Y. Liu, B. Wang, F. Lei, L. Li, A. W. M. Chan, L. Xu, Y. Shi, Y. Du, W. Hao, P. K. Wong, J. Wang, S. X. Dou, L. Zhang, J. C. Yu, *J. Am. Chem. Soc.* **2020**, *142*, 7036; b) A. Mencio, J. Mas-Pla, N. Otero, O. Regas, M. Boy-Roura, R. Puig, J. Bach, C. Domenech, M. Zamorano, D. Brusi, A. Folch, *Sci. Total Environ.* **2016**, *539*, 241.
[5] L. Huang, L. Cheng, T. Ma, J. J. Zhang, H. Wu, J. Su, Y. Song, H. Zhu, Q. Liu, M. Zhu, Z. Zeng, Q. He, M. K. Tse, D. t. Yang, B. I. Yakobson, B. Z. Tang, Y. Ren, R. Ye, *Adv. Mater.* **2023**, *35*, 2211856.

[6] a) Y. Wang, W. Zhou, R. Jia, Y. Yu, B. Zhang, *Angew. Chem., Int. Ed.* **2020**, *59*, 5350; b) R. Daiyan, T. Tran-Phu, P. Kumar, K. Iputera, Z. Tong, J. Leverett, M. H. A. Khan, A. Asghar Esmailpour, A. Jalili, M. Lim, A. Tricoli, R-S. Liu, X. Lu, E. Lovell, R. Amal, *Energy Environ. Sci.* **2021**, *14*, 3588; c) Y. Fu, S. Wang, Y. Wang, P. Wei, J. Shao, T. Liu, G. Wang, X. Bao, *Angew. Chem., Int. Ed.* **2023**, *62*, 202303327; d) W. Wang, J. Chen, E. C. M. Tse, *J. Am. Chem. Soc.* **2023**, *145*, 26678.

[7] T. Zhu, Q. Chen, P. Liao, W. Duan, S. Liang, Z. Yan, C. Feng, *Small* **2020**, *16*, 2004526.

[8] a) Y. Shi, Y. Li, R. Li, X. Zhao, Y. Yu, M. Yang, *Chem. Eng. J.* **2024**, *479*, 147574; b) Z. Shen, J. Yan, M. Wang, L. Xing, B. Huang, H. Zhou, W. Li, L. Chen, J. Shi, *ACS Sustainable Chem. Eng.* **2023**, *11*, 9433.

[9] J.-Y. Fang, Q.-Z. Zheng, Y.-Y. Lou, K.-M. Zhao, S.-N. Hu, G. Li, O. Akdim, X.-Y. Huang, S.-G. Sun, *Nat. Commun.* **2022**, *13*, 7899.

[10] a) B. Liu, S. Zhan, J. Du, X. Yang, Y. Zhao, L. Li, J. Wan, Z. J. Zhao, J. Gong, N. Yang, R. Yu, D. Wang, *Adv. Mater.* **2023**, *35*, 2206450; b) L. Zhang, W. Yi, J. Li, G. Wei, G. Xi, L. Mao, *Nat. Commun.* **2023**, *14*, 6318.

[11] K. Ma, J. Wu, X. Wang, Y. Sun, Z. Xiong, F. Dai, H. Bai, Y. Xie, Z. Kang, Y. Zhang, *Angew. Chem., Int. Ed.* **2022**, *61*, 202211094.

[12] Y. Fang, Y. Liu, L. Qi, Y. Xue, Y. Li, *Chem. Soc. Rev.* **2022**, *51*, 2681.

[13] X. Feng, J. Liu, L. Chen, Y. Kong, Z. Zhang, Z. Zhang, D. Wang, W. Liu, S. Li, L. Tong, J. Zhang, *J. Am. Chem. Soc.* **2023**, *145*, 10259.

[14] Y. Kong, J. Li, S. Zeng, C. Yin, L. Tong, J. Zhang, *Chem* **2020**, *6*, 1933.

[15] Y. Kong, X. Li, L. Wang, Z. Zhang, X. Feng, J. Liu, C. Chen, L. Tong, J. Zhang, *ACS Nano* **2022**, *16*, 11338.

[16] H. Shang, Z. Zuo, L. Yu, F. Wang, F. He, Y. Li, *Adv. Mater.* **2018**, *30*, 1801459.

[17] J. Wu, J. Liu, J. Liang, Y. Zhang, X. Zhao, C. Yuan, *Phys. Chem. Chem. Phys.* **2022**, *25*, 69.

[18] G. Ma, O. A. Syzgantseva, Y. Huang, D. Stoian, J. Zhang, S. Yang, W. Luo, M. Jiang, S. Li, C. Chen, M. A. Syzgantseva, S. Yan, N. Chen, L. Peng, J. Li, B. Han, *Nat. Commun.* **2023**, *14*, 501.

[19] Y. Ma, J. Hou, *Int. J. Mol. Sci.* **2022**, *23*, 8421.

[20] a) Q. Zhu, K. Zhu, M. Cai, Y. Zhang, Z. Shao, M. Jiang, X. Wang, Z. Geng, X. Wu, M. Li, K. Huang, S. Feng, *Nano Res.* **2022**, *15*, 7099; b) W. Xue, X. Liu, C. Liu, X. Zhang, J. Li, Z. Yang, P. Cui, H. J. Peng, Q. Jiang, H. Li, P. Xu, T. Zheng, C. Xia, J. Zeng, *Nat. Commun.* **2023**, *14*, 2137.

[21] R. Zhao, Q. Yan, L. Yu, T. Yan, X. Zhu, Z. Zhao, L. Liu, J. Xi, *Adv. Mater.* **2023**, *35*, 2306633.

[22] Y. Wang, Y. Xu, C. Cheng, B. Zhang, B. Zhang, Y. Yu, *Angew. Chem., Int. Ed.* **2023**, *63*, 202315109.

[23] J. Ma, Y. Zhang, B. Wang, Z. Jiang, Q. Zhang, S. Zhuo, *ACS Nano* **2023**, *17*, 6687.

[24] a) T. Ren, K. Ren, M. Wang, M. Liu, Z. Wang, H. Wang, X. Li, L. Wang, Y. Xu, *Chem. Eng. J.* **2021**, *426*, 130759; b) C. Wang, Z. Liu, T. Hu, J. Li, L. Dong, F. Du, C. Li, C. Guo, *ChemSusChem* **2021**, *14*, 1825; c) H. Wang, Y. Guo, C. Li, H. Yu, K. Deng, Z. Wang, X. Li, Y. Xu, L. Wang, *ACS Appl. Mater. Interfaces* **2022**, *14*, 34761; d) D. Yin, D. Chen, Y. Zhang, W. Wang, Q. Quan, W. Wang, Y. Meng, Z. Lai, Z. Yang, S. Yip, C. Y. Wong, X. Bu, X. Wang, J. C. Ho, *Adv. Funct. Mater.* **2023**, *33*, 2303803; e) M. He, R. Chen, Y. Zhong, H. Li, S. Chen, C. Zhang, S. Deng, F. Gao, *Colloids Surf., A.* **2024**, *681*, 132746; f) Y. Gao, H. Liu, Z. Zheng, X. Luan, Y. Xue, Y. Li, *NPG Asia Mater.* **2023**, *15*, 12; g) X. Luan, Z. Zheng, S. Zhao, Y. Xue, Y. Li, *Adv. Funct. Mater.* **2022**, *32*, 2202843; h) S. Zhao, Z. Zheng, L. Qi, Y. Xue, Y. Li, *Small* **2022**, *18*, 2107136; i) X. Zheng, Y. Xue, C. Zhang, Y. Li, *CCS Chem.* **2023**, *5*, 1653.